World Electric Vehicle Journal

MDPI

Article

A Six Legs Buck-boost Interleaved Converter for KERS Application

Gianpaolo Vitale [1,*] and Emiliano Pipitone [2]

[1] ICAR, Institute for high performance computing and networking, National Research Council of Italy, via Ugo La Malfa 153, Palermo, Italy
[2] Department of Engineering, University of Palermo, Viale delle Scienze, Palermo, Italy; emiliano.pipitone@unipa.it
* Correspondence: gianpaolo.vitale@icar.cnr.it;

Received: 20 March 2019; Accepted: date; Published: date

Abstract: An electric Kinetic Energy Recovery System for Internal Combustion Engine Vehicles is proposed. The system employs a supercapacitor (SC) as storage system and a motor generating unit (MGU) connected to the drive shaft for vehicle acceleration and braking: a suitable power converter is hence needed to adequately manage energy exchange between the two elements. This paper describes in particular the design of the bidirectional DC/DC power converter to interface SC and MGU using available commercial devices thus obtaining a cheap and high efficiency conversion. These requirements are obtained by an interleaved six legs topology in which the current is shared among six inductors to minimize their weight and cost. It is shown that its design criteria differ from traditional interleaved converters. The same topology allows the input and output ripple to be minimized improving the reliability in case of fault. Losses are reduced both by sharing the currents and by a suitable control strategy which allows more converters to be connected in parallel to increase the delivered power. Results given in simulation assess the stability and dynamic performance of the conversion circuit showing a very low current and voltage ripple in operating conditions.

Keywords: Hybrid Vehicle; Urban Driving Cycle; Kinetic Energy Recovery System; KERS; Supercapacitor; Vehicle Fuel economy; Regenerative Braking

1. Introduction

Sustainable mobility development requires the exploration of new solutions to reduce fuel consumption and to respect environment. Among these, a growing attention is addressed to road transport emission and urban pollution [1-2], to the advances in combustion optimization [3] and control [4] of alternative and cost effective fuels, as well as the optimal management of vehicles drive-line [5-6]. Nevertheless, one of the heaviest lack of traditional internal combustion engine vehicles (ICEV) is the huge amount of energy lost by friction during the braking phases. This energy, suitably recovered, could be efficiently employed during acceleration contributing to lower the energy consumption of the vehicles and the related pollution.

Several Regenerative Braking Systems (RBS) or Kinetic Energy Recovery Systems (KERS) have been studied and optimized for different kind of vehicles (Electric, Hybrid or Internal combustion engine vehicle), equipped with energy storage system of different kind (mechanical, electrical, chemical, hydraulic), and suitable or not for retrofit application on current production vehicles. In Hybrid Electric Vehicles (HEV), as well as in pure Electric Vehicles (EV), the presence of powerful generator and/or motor interfaced to high capacity energy storage allows the easy implementation of regenerative braking, using fuel cells, battery, or supercapacitors as storage systems.

Recently the so called starter–generator systems have been considered for vehicle powering in starting and generating functions; their growth, both in power and control complexity and encompass launching ability, could improve the hybridization on all vehicles thanks to the reduction of the cost of power electronics and other related technologies [7]. The use of battery as storage system has been considered for example in [8, 9, 10]. Now the development of advanced storage systems as supercapacitors has been assessed to manage the energy exchange in extreme braking conditions [11] . Usually SCs are used together with traditional battery [12 -13] where they are being strategic to manage the energy storage by buffering the battery during power transients and enabling greater acceleration and regenerative braking capabilities. The voltage adaptation between the starter/generator and/or the battery is performed by suitable power converters able to guarantee a bidirectional flow of energy and high conversion efficiency [12, 14]. Differently from the above mentioned papers, the proposed approach considers only SCs to exchange energy with the starter–generator aiming to obtain a cheaper plug-in system to be used in large diffusion internal combustion engine vehicles for urban transportation.

The use of supercapacitors (SCs) as fast and efficient energy storage solution in power application is widely recognized since they offer higher power densities with respect to traditional batteries, and energy densities from 10 to 20 times higher than electrolytic capacitors. The so-called Double-Layer-Capacitors (DLCs) are available on the market with capacitance values up to 1500 F; even if the voltage of a single unit is low (about 2.7 V) higher rated voltages are obtained by suitable series-parallel arrangements [15]. One of the major drawbacks of this technology consists on its low volumetric and gravimetric energy density in comparison with batteries or fuel cells. However DLCs become an interesting option when highly dynamic charging or discharging profiles are concerned, with high current rates [16]. This is because of their exceptional high power capabilities (specific power densities up to about 3400 W/kg and specific energy up to 30 Wh/kg, and life cycles of up to 10^6) [17].

Unlike electrified vehicles, Internal Combustion Engine Vehicles (ICEV) are not equipped with generator, motor and batteries of adequate power and capacity to perform regenerative braking; for these kind of vehicles, hence, mechanical, hydraulic or pneumatic energy storage devices [18] has been proposed to recover the vehicle kinetic energy during braking phases. A comparison among regenerative braking systems is proposed in [19] where it is underlined that the electric energy recovery systems suffer both of losses of energy due to energy transformations and long recharging times. On the other hand, Hydraulic/Pneumatic based solutions exhibit a limited energy storage and for flywheels based systems a loss of rotational energy over time due to friction and air resistance is noticeable. The proposed approach aims to improve the efficiency of the power conversion chain in electric KERS by a suitable design of the DC/DC converter and adopting supercapacitors as storage units. In particular the system presented in this paper is intended for the application to ICEV and is composed by a SC interfaced to a motor-generator unit (MGU) through a power converter, whose function is to adapt the voltage levels between SC and MGU during operation. This paper analyses the design of a Buck-boost power converter able to manage the electric power transfer energy exchange between the SC and the MGU. It is shown that the efficiency of the DC/DC converter plays a key role since the power is processed twice. Its main features are the modularity and efficiency achieved minimizing the cost of the hardware.

2. The KERS Operating Principle

The Kinetic Energy Recovery System (KERS) considered in this work, is composed of a supercapacitor (SC), which is the energy storage of the system, electrically interfaced, through the power converter (PC) developed in this paper, to the motor generator unit (MGU), which is mechanically connected to the drive shaft, and then to the wheels, via a fixed gear ratio.

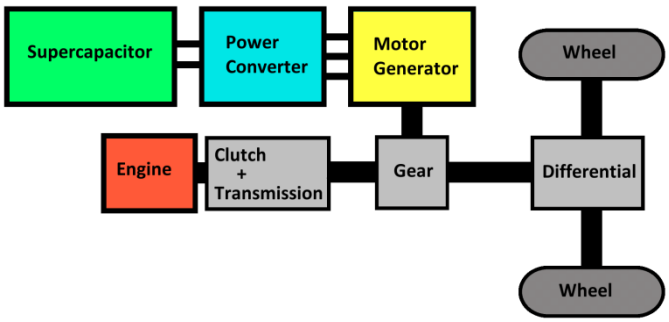

Figure 1. Schematic representation of the KERS.

During braking phases, the MGU converts the vehicle kinetic energy coming from the drive shaft into electric energy; the power converter has to operate the necessary conversion (varying voltage and current) to transfer this energy to the SC. On the contrary during acceleration, the SC delivers energy to the power converter that supplies the MGU which contributes to vehicle propulsion through the drive shaft.

The whole system hence is bidirectional, thus allowing the mechanical energy to be converted into electrical energy (braking) and vice versa (acceleration). The power converter comprises two stages: a DC/DC and a DC/AC. This paper is focused on the design of the DC/DC stage, it is connected to the SC and to the DC/AC inverter of the MGU. Since usually the SC voltage is lower than the voltage at the DC/AC, the DC/DC converter will be operated in boost mode (increasing the voltage of the SC to supply the inverter) during acceleration, or in step-down mode (lowering the voltage of the DC/AC to charge the SC) during braking.

3. DC/DC Converter Constraints Design

The voltage of the storage system and of the MGU are two constraints for the DC/DC converter together with the rated power. They depend on the vehicle and on its performance during braking and acceleration.

3.1. The Supercapacitor Based Storage System

The Supercapacitor based storage system has been chosen on the basis of the New European Driving Cycle (NEDC), it consists of four repetitions of the urban cycle ECE-15 and one of extra-urban cycle EUDC [20].

The energy delivered from the SC bank to the MGU has been calculated in the worst case for a compact car whose mass is equal to about 980 kg, and corresponds to a peak of 10,3 kW reached at the end of the acceleration taken during the cycle ECE-15 as shown in figure 2.

$$E_{acc} = \int_t Pdt = 32.9\,Wh \tag{1}$$

The energy received during braking can be calculated in the same way. From figure 3 the maximum power reaches 6 kW and the energy to be stored is given by:

$$E_{brak} = \int_t Pdt = 3.33\,Wh \tag{2}$$

On this basis the Maxwell SC Unit BMOD0083 P048 has been chosen. Its main features are:

- Rated Capacitance: 83 F
- Maximum ESRDC, initial: 10 mΩ
- Rated Voltage: 48 V
- Absolute Maximum Voltage: 51 V
- Absolute Maximum Current: 1150 A

This SC unit is able to deliver 26.5 Wh. This value is slightly lower than that calculated with (1).

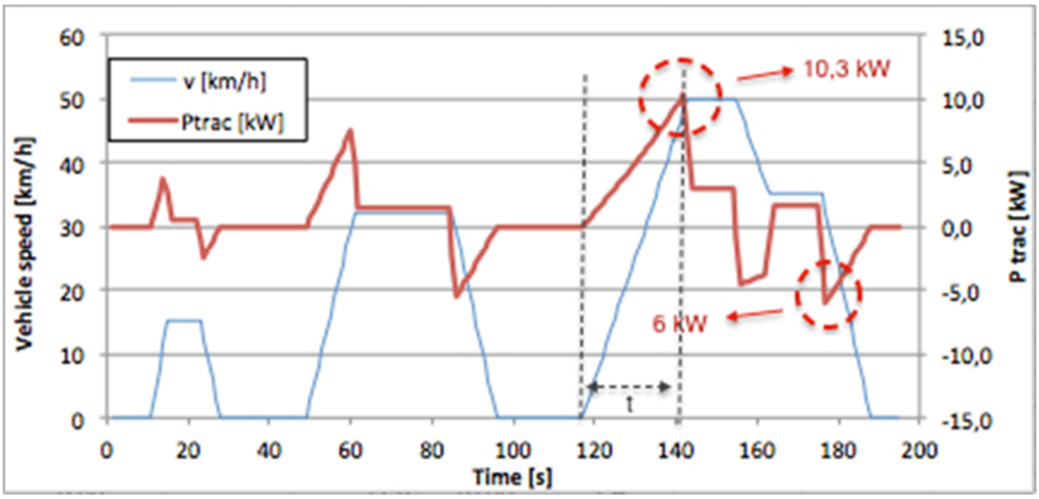

Figure 2. Speed and power for the urban vehicle under study.

3.2. The Motor Generator Unit

The MGU has to guarantee the conversion from mechanical to electric energy and vice versa. It has been chosen considering the peak of the power. The MGU Motenergy ME0201013601 has been chosen. This motor exhibits an efficiency equal to 92% at DC voltage from 12V to 96V and a continuous current of 60A. This is a 3-phase, Y-connected Permanent Magnet Synchronous Motor with an axial air gap. The maximum rotor speed is equal to 5000 rpm. The continuous output power is 5 kW at 96 VDC at 4400 rpm and can deliver a peak output for 1 minute of 13 kW. This feature is compatible with the duration of the acceleration phase shown in figure 3. This kind of motor allows the voltage at the output of the DC/DC converter to be fixed to 98V. This slight increase compared to the maximum rated voltage compensates the voltage drop at high currents due to parasitic resistance of electric contacts. It can be noted that as much higher is the operating voltage as lower will be the current so to lessen ohmic losses.

4. Design of the DC/DC converter

As far as the topology is concerned, the interleaved structure has been selected since it offers a good efficiency and a reduced ripple on the current. Moreover it assures a high reliability since it can be operated with a reduced number of legs in case of failure [21-22]. In particular a six legs structure has been considered as shown in Figure 3.

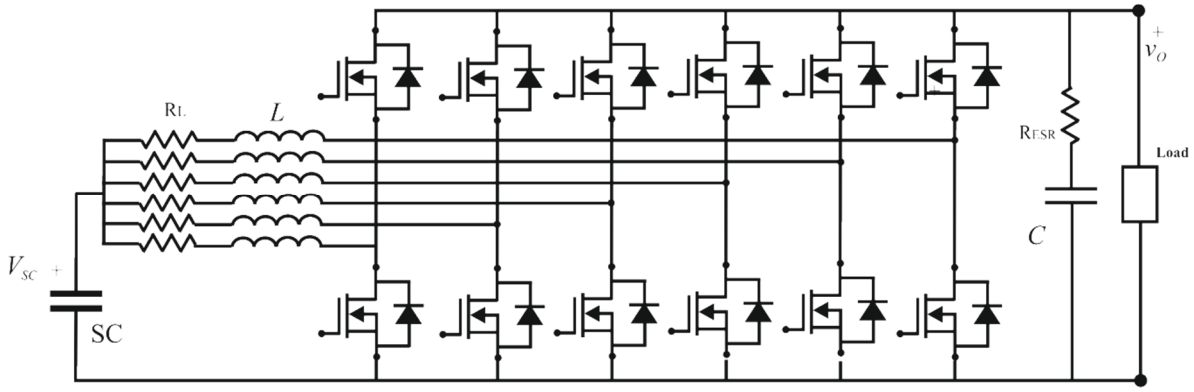

Figure 3. Electric scheme of the six-legs interleaved converter.

This converter behaves as a Buck or a Boost depending on the devices operated. In particular the boost mode is obtained for each leg by switching the bottom Mosfet and top with the top Mosfet idle as shown in figure 4.

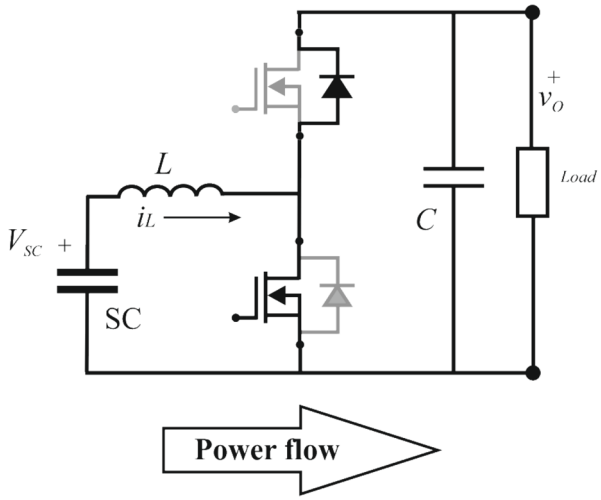

Figure 4. Electric scheme of one leg of the interleaved DC/DC converter in boost operation.

The inductor has been designed considering a switching frequency of 20 kHz to assure low switching losses in the power devices, and a maximum ripple of the current of 3A peak-to-peak. The design is performed to maintain the converter operating in Continuous Conduction Mode (CCM) so that the current flows through the inductor without interruption during the switching period. The threshold value of inductor to assure the CCM is calculated in the worst case represented by the ratio value of the time interval in which the power switches is in conduction state divided by the switching period or duty cycle (D) equal to 0.5 and is given by:

$$L_{CCM} = \frac{Vo(1-D)D}{\Delta I_L \, f_s} = 408\mu H \tag{3}$$

Where f_s is the switching frequency, Vo is the output voltage and ΔI_L is the maximum peak-to-peak variation of the input current. The current flowing through the inductor is composed of a DC value and of a triangular shaped AC component superimposed. In order to assure the CCM operation the DC value must be greater than one half of ΔI_L.

A 500μH inductor is chosen considering a tolerance up to 20%. It is reasonable to assume a maximum current of 10 A to maintain the cost as low as possible, hence a DC current of 8.5 A is admitted; on this basis the rated power of the six leg converter corresponds to about 2400W. A higher power can be obtained employing more converters in parallel as it will be shown later.

In the following part of the paper, the analysis of a single module with 2400W of rated power will be carried out.

The output capacitor is designed considering D≈1 as worst case and an output voltage ripple ΔVo of 3%. It results:

$$C = \frac{D}{R \, f_s \, (\Delta V_0 / V_0)} = 416\mu F \tag{4}$$

A commercial value of 560 uF is chosen allowing a ripple of about 2.2% considering a load resistance of 4Ω as the worst case.

As far as the power switches are concerned, a CoolMOS type with 25 A of rated current is selected. The design constraints of the converter are summarized in table 1 and the list of the commercial devices including parasitic components is given in table 2.

Table 1. Constraints Design of the DC/DC converter.

Parameter	Symbol	Value
Input voltage	V_{SC}	48 V
Output voltage	V_o	96 V
Number of legs	N	6
Rated power	P_{conv}	2400 W
Maximum ripple of the current in a leg	ΔI_L	3 A
Maximum current in a leg	I_L	10 A
Switching frequency	f_s	20 kHz

Table 2. Commercial components of the six legs interleaved converter.

Electrical symbol	Rated value	Supplier	Code
L	I_L = 10 A, L = 500 uH, R_L = 50 mΩ	Vishay	IHV15BZ500
C	560 μF, Resr = 160 mΩ	Epcos	B43511A4567M007
MOSFET	V_{DSS} = 650 V, R_{DS}(on) = 110 mΩ@25 °C; I_{DS} = 25 A	Infineon Technologies	IPA60R125CP CoolMOS

5. Efficiency evaluation

The efficiency has been obtained by evaluating the losses versus the current in each device. The losses depend in different way on the current, they can be constant, linear quadratic with the current, hence it is expected that the efficiency curve will exhibit a maximum [23]; unfortunately during KERS operation, the power transferred between SC and MGU is required to vary appreciably; for this reason, a proper control strategy has been conceived to maximize the converter efficiency apart from the power involved.

The following losses have been considered: a) switching losses on Mosfet devices, b) conduction losses on Mosfet devices, c) conduction losses on a diode, d) diode recovery losses on a diode, e) Joule losses on the parasitic resistance of the inductor and magnetic losses, f) magnetic losses, g) Joule losses on the parasitic resistance of the output capacitor.

The losses have been firstly evaluated for a unique leg operated in the worst case meaning with rated current and D=0.5. The switching losses for a single Mosfet device at rated current of I=10A and V=98 V are:

$$P_{SW} = \frac{1}{2} V\, I\, (t_{on} + t_{off}) f_s \cong 0.1\, W \tag{5}$$

Where for the selected Mosfet t_{on}=t_{off}=5ns. The conduction losses on a Mosfet are:

$$P_c = D\left[R_{ds(ON)} \left(\bar{I}_L^{\,2} + \frac{\Delta I_L^2}{12} \right) \right] = 7.3\, W \tag{6}$$

Where the root mean square of the current has been calculated as the sum of the maximum DC value equal to 8.5A and the AC components which is a triangular waveform with ΔI_L=3A.

The power loss on the diode are calculated considering the conduction and the recovery losses:

$$P_{D\_cond} = D\left[V_\gamma \bar{I}_D + R_D \left(\bar{I}_D^{\,2} + \frac{\Delta I_L^2}{12} \right) \right] = 0.05W \tag{7}$$

$$P_{D\_rr} = \frac{1}{2} V t_{rr}\, I_{rr} f_s = 17.3W \tag{8}$$

Where t_{rr} = 430 ns, I_{rr} = 42 A.

198 The power loss on one inductor can be calculated on the basis of the square of rms value of the
199 current multiplied for the parasitic resistance.

$$P_L = R_L\left(\bar{I}_D{}^2 + \frac{\Delta I_L^2}{12}\right) = 3.65\,W \quad \textbf{(9)}$$

200 The magnetic losses have been calculated by the Revised Generalized Steinmetz Equation
201 (RGSE) following the methods explained in [24] obtaining 0.2W for each core.
202 The power loss on output capacitor in the worst case is given by:

$$P_{C\_C} = R_{ESR}(1-D)I_{rms}^2 = R_{ESR}(1-D)\left(\frac{\Delta I_L}{2\sqrt{3}}\right)^2 = 0.06\,W \quad (10)$$

203 Where I_{rms} is the root mean square value of the AC current flowing through the capacitor equal to
204 0.87A.

205 **Table 3.** Power losses and efficiency calculation at rated power.

Loss	Value [W]
Mosfet switching losses (x6)	0.6
Mosfet conduction losses (x6)	43.8
Diode conduction losses(x6)	0.3
Diode reverse recovery losses (x6)	104
Inductor joule losses (x6)	21.9
Inductor magnetic losses (x6)	1.2
Capacitor losses	0.06
TOTAL LOSSES	171.86

206 At the rated power of 2400 W, the theoretical efficiency results equal to 92.8%. The equations
207 (5-8) have been implemented versus the output current, then the converter efficiency has been
208 analyzed considering the operation of two, three, four, five and six legs with the output current as
209 parameter. Each leg is operated so that the modulating carrier are shifted in phase of $2\pi/N$, where N
210 is the number of operated legs. In this way the ripple in the input and output current will be reduced
211 as well as the current through the output capacitor minimizing the losses on R_{esr}. The frequency of
212 the ripple results higher (equal to 120kHz when all legs are operated) making easier the harmonic
213 filtering [25].
214 The ripple on the input current depends on the duty cycle and on the number of operated legs.
215 The analysis of the reduction of the current ripple in interleaved operation mode can be carried out
216 by calculating the cancellation factor KI as the ratio between the input ripple ΔI and the current
217 ripple of each inductor ΔI_L as in (10) for N=2,3,4,… [26].

$$KI = \frac{\Delta I}{\Delta I_L} = N\frac{\prod_{i=1}^{N-1}\left|\frac{i}{N} - D\right|}{\prod_{i=1}^{N-1}\left(\left|\frac{i}{N} - D\right| + \frac{1}{N}\right)} \quad (11)$$

218 This value is shown in figure 5 where it can be noted that, for example, when four legs are
219 operated the complete cancellation is obtained for D=0.25 and D=0.75.

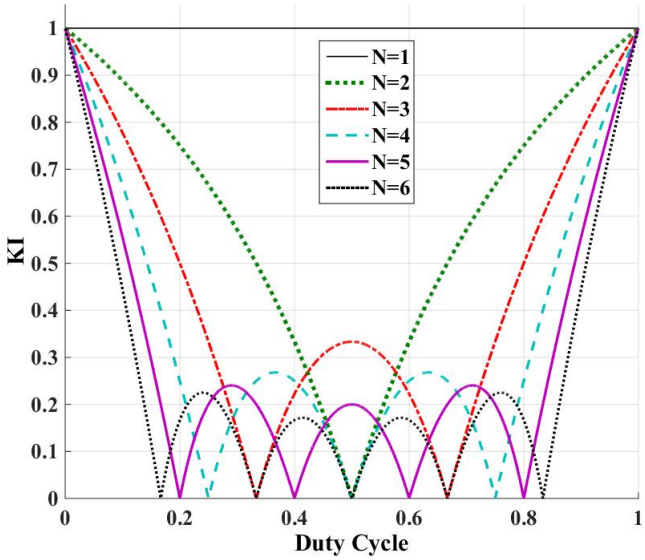

Figure 5. Cancellation Factor versus duty cycle.

It can be noted that a three-leg converter gives a good ripple cancellation factor; literature highlights that reduction is not significant for more than four legs and the number of circuit components increases; for the KERS purposes anyway is appropriate that the number of the legs is augmented to six with the aim to adopt cheaper inductors and to improve the efficiency as explained hereinafter. Moreover this guarantees a redundancy in case of failure of a leg, thus also improving the reliability of the converter [26]. Figure 6 shows the efficiency calculated considering a number of operated legs from one to six versus the input power. It can be observed that each curve exhibits a maximum in different locations. In order to obtain a high and flat efficiency curve, the control strategy is designed to operate only the first leg up to input power of about 500W, two legs are operated from 500W up to about 900W and so on until the maximum power is reached according to (12). This strategy allowed to obtain the efficiency curve represented in figure 7. It can be noted that the efficiency at rated power calculated by simulating the converter in real operating condition, shown in figure 6 for six legs operated, gives 93.2% confirming the theoretical worst case analysis shown in table 3.

$$operated\ legs: \begin{cases} 0 < P \le 516 & leg \quad 1 \\ 516 < P \le 906 & legs \quad 1,2 \\ 906 < P \le 1268 & legs \quad 1,2,3 \\ 1268 < P \le 1664 & legs \quad 1,2,3,4 \\ 1664 < P \le 2001 & legs \quad 1,2,3,4,5 \\ 2001 < P \le 2400 & legs \quad 1,2,3,4,5,6 \end{cases} \tag{12}$$

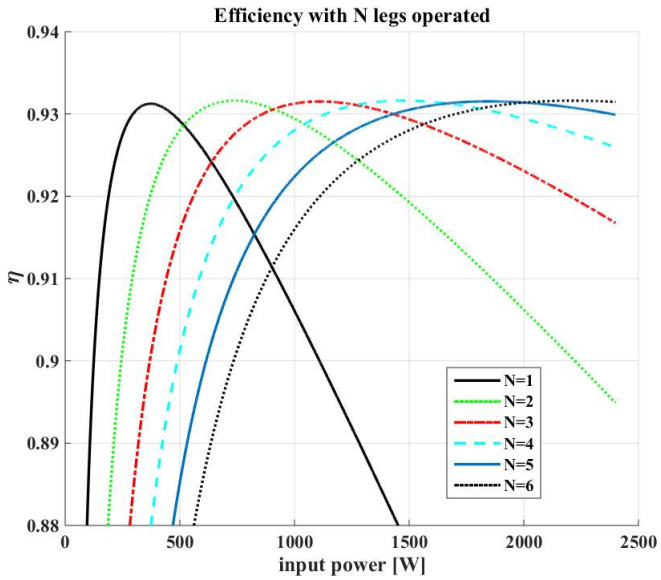

Figure 6. Comparison of the efficiency for each group of legs operated.

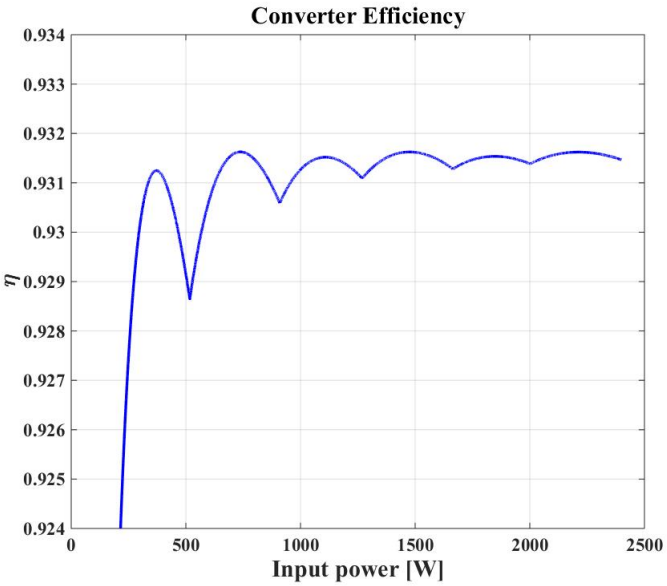

Figure 7. Total efficiency of the interleaved converter.

6. Control Strategy

The control algorithm is based on a voltage loop, to maintain constant the output voltage, and on a current loop. On the basis of the voltage error processed by a PI regulator the reference current is obtained, it is compared with the current given by the converter, then another PI regulator calculates the value of the duty cycle. The number of operated legs is defined by the reference current that depends on the power required or delivered by the SC bank. The current control imposes the reference current in each inductor avoiding the circulation of parasitic currents. In addition this feature allows more converters to be connected in parallel to increase the output power. The carrier signals are shifted in phase on the basis of the number of legs to be operated, in this way the input and output ripple will be minimized resulting with a frequency much higher than the witching frequency of each leg. The block diagram of the control system is sketched in Figure 8.

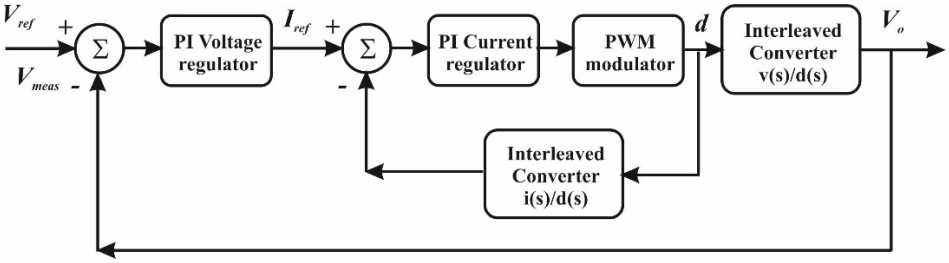

Figure 8. block diagram of the control system.

The two transfer functions giving the voltage and the current versus the duty cycle are [27]:

$$G_v(s)=\frac{\tilde{v}_o(s)}{\tilde{d}(s)}=\frac{s\cdot(-R_L L i_L)+RV_{DC}(1-D)-RR_L i_L}{s^2\cdot RLC+s\cdot(L+RR_L C)+R_L+R(1-D)^2} \quad (13)$$

$$G_{iL}(s)=\frac{\tilde{i}_L(s)}{\tilde{d}(s)}=\frac{s\cdot V_{DC}RC+R(1-D)i_L+V_{SC}}{s^2\cdot RLC+s\cdot(L+RR_L C)+R_L+R(1-D)^2} \quad (14)$$

The two PI regulators have been properly designed, choosing

$$PI_i(s)=101.8\cdot[(1+0.00012/s)/s] \quad (15)$$

for the current control loop, and

$$PI_v(s)=742.8\cdot[(1+0.0014/s)/s] \quad (16)$$

for the voltage control loop; a gain margin of 12 dB and a phase margin of 70° is assured for the open loop transfer function G(s):

$$G(s)=PI_V(s)\frac{PI_i(s)}{1+PI_i(s)\cdot G_{iL}(s)}G_v(s) \quad (17)$$

The closed loop transfer function obtained by (16) shows a dominant negative real part pole p1= -0.028 rad/s and a couple of complex conjugate poles p2,3= -0.2502 ±j 1.3082 giving an overdamped response of the output voltage.

7. Results

Simulation results have been carried out to verify the main features of the designed converter: the reduced ripple of the current and the dynamic performances. Figure 9 shows a steady state test at rated power. Albeit the currents on the six inductors exhibit a period of 50 μs (corresponding to the switching frequency of 20 kHz) the current supplied by the supercapacitor has a period of 8.33 μs (corresponding to a fundamental frequency of 120 kHz) and a ripple of 0.35%. The load voltage experiences the same period and a ripple of 1.53%. In figure 10 a dynamic test obtained by varying the load from 4Ω to 12Ω at t=0.1s is shown. It can be noted that, after the load reduction, the slope of the voltage of the supercapacitor is lessened as expected. The current supplied by the supercapacitor after a transient of about 10 ms reaches the new value and the voltage on the load is maintained to 98 V by the control system.

A test by varying the reference voltage from 80 V to 98 V at t=0.03s is sketched in figure 11. The output voltage requires only about 50 ms to reach the new value and the transient is overdamped as calculated in section 6. Both the load voltage and the supplied current exhibit a reduced ripple. In particular for the output voltage ripple is equal to 1.5 V peak-to-peak when the DC output is 98 V and the ripple of the supplied current is equal to 0.35A peak-to-peak when the DC current is 33A.

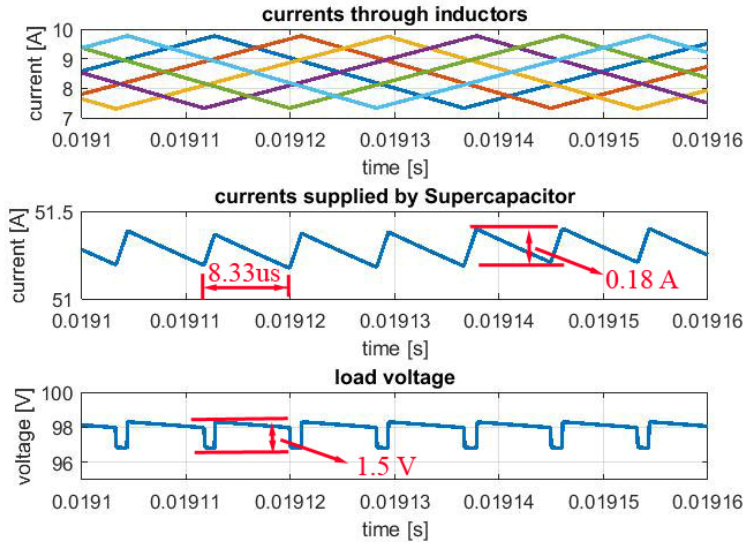

277

278 **Figure 9.** steady state test at rated power: currents through inductors (top), current supplied by the
279 supercapacitor (middle), load voltage (bottom).

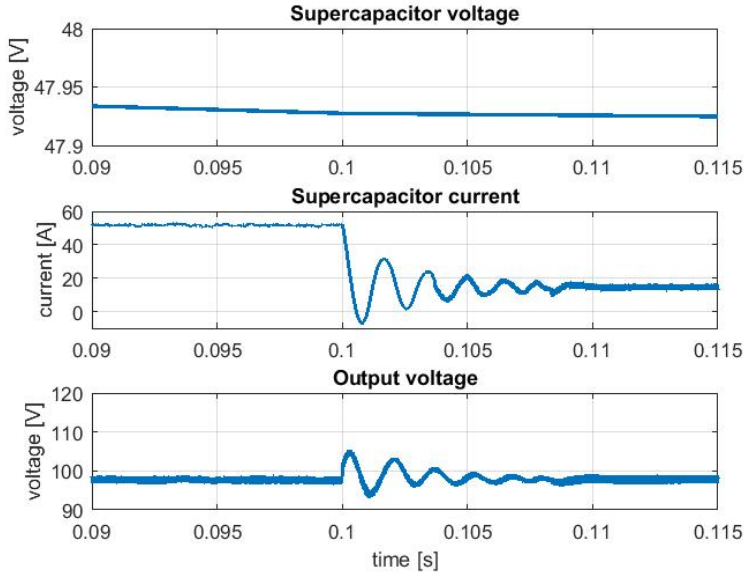

280

281 **Figure 10.** dynamic test with load variation: supercapacitor voltage (top), current supplied by the
282 supercapacitor (middle), load voltage (bottom).

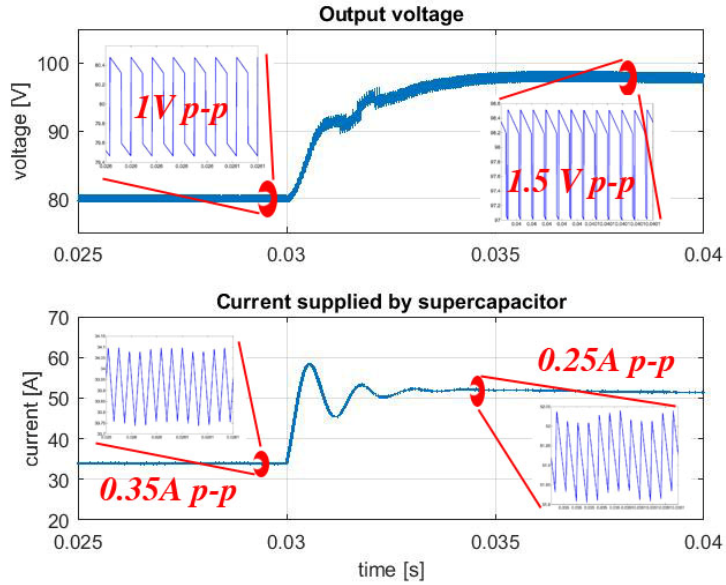

Figure 11. dynamic test with reference output voltage variation: output voltage (top), current supplied by the supercapacitor (bottom).

A final test is carried out to reproduce the current required for the 20s acceleration phase sketched in figure 3 during which the power rises up to 10.3 kW. Firstly the operating condition of a single power module has been reproduced considering the power rising from zero to 2.4 kW in 4s corresponding to a single DC/DC converter unit. Figure 12 shows the power delivered to the MGU and the output voltage of the DC/DC converter; it can be noted that the voltage ripple remains low even near to the rated power. In figure 13 the current delivered by the SC and the voltage at the terminals of the SC are drawn. Also in this case a low current ripple can be appreciated.

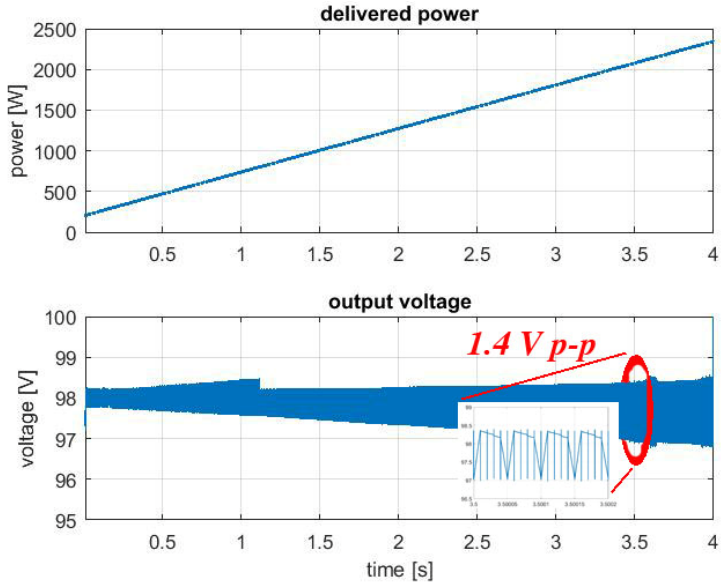

Figure 12. acceleration test: power delivered to the MGU (top), output voltage (bottom).

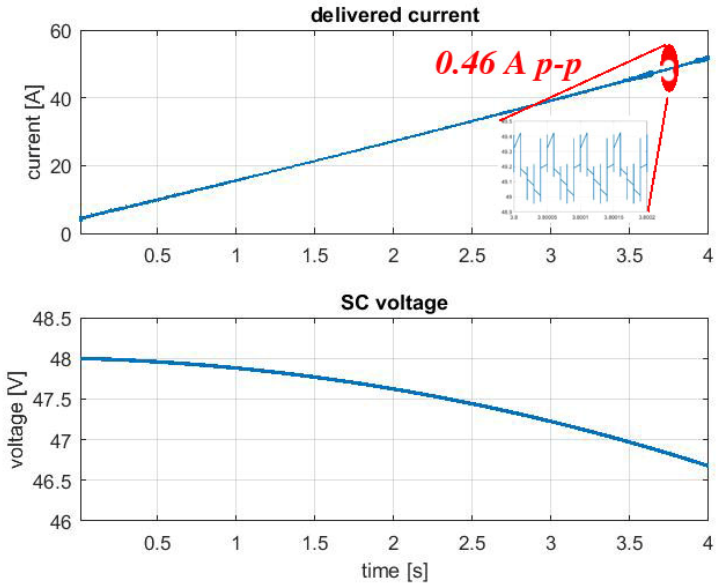

Figure 13. acceleration test: current delivered by the supercapacitor (top), supercapacitor voltage (bottom).

In order to satisfy the whole power requirements, five power converter parallel connected have to be employed as shown in figure 14. Each converter is supplied by the supercapacitor bank SC and delivers power to the DC/AC conversion unit of the MGU drive. Each converter is operated in a range of 4s till to reach the maximum required power. In order optimize the efficiency of the system, each converter is started when the previous unit is operating at rated power i.e. when its efficiency is near to the maximum value. The waveforms of the current for each DC/DC converter and the total current delivered to the MGU drive are shown in figure 15.

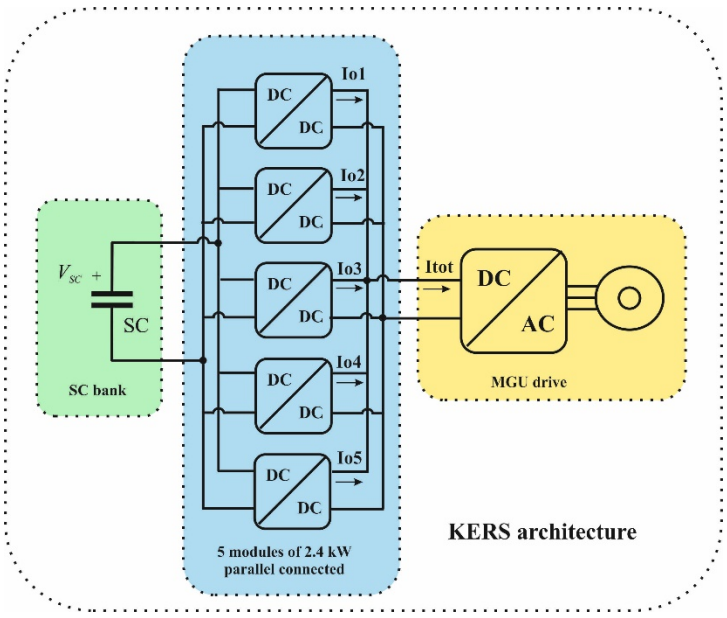

Figure 14. Schematics of the KERS architecture.

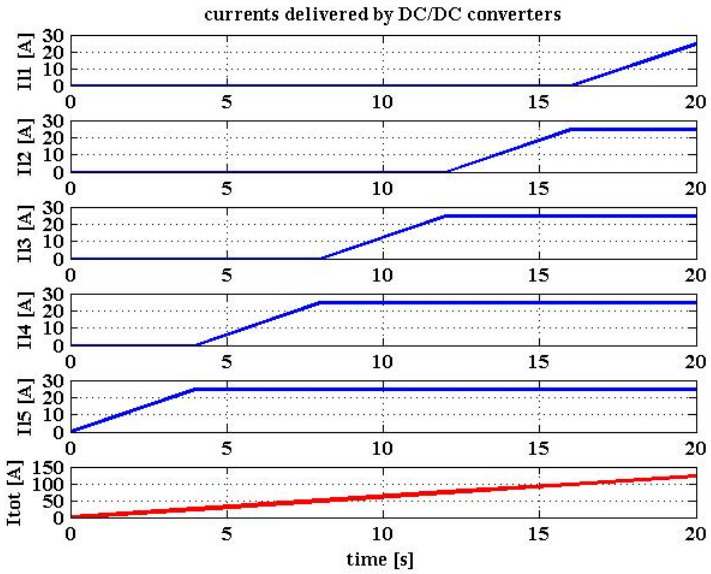

Figure 15. current delivered by DC/DC converters and total current during an acceleration transient.

It can be noted that the control system is able to manage the power requirements and after that a converter reaches its nominal power the next is started.

8. Conclusions

A six legs interleaved converter has been designed to manage the power transfer between the elements of an electric KERS proposed for internal combustion engine vehicles. The system is conceived to allow a significant saving of fuel, and consequent CO_2 reduction, in urban area. The analysis has been performed considering commercial devices aiming to obtain a cheap realization so that it can be used in low cost vehicles. Differently from traditional interleaved converter a greater number of legs has been chosen to guarantee a higher efficiency and reliability. The number of legs assures a flat efficiency curve by a suitable choice of the number legs simultaneously operated according the required power. The stability is assessed by a control strategy based on a voltage and a current loop. Steady state output current and voltage exhibit a very low ripple despite the low switching frequency. Finally the modularity of the proposed solution allows arbitrarily greater power to be managed.

Acronyms and symbols

CCM	Continuous Conduction Mode
DLC	Double Layer Capacitor
ESRDC	Parasitic resistance of the supercapacitor
EUDC	Extra-Urban Cycle
EV	Electric Vehicle
HEV	Hybrid Electric Vehicles
ICEV	Internal Combustion Engine Vehicle
KERS	Kinetic Energy Recovery Systems
MGU	Motor Generating Unit
NEDC	New European Driving Cycle
PC	Power Converter
RBS	Regenerative Braking Systems
RGSE	Revised Generalized Steinmetz Equation
SC	supercapacitor
C	Output capacitor of the six-legs DC/DC converter
D	Duty cycle of the power switch of the six-legs DC/DC converter
Δi_L	Peal-to-Peak current variation in an inductor of the six-legs DC/DC converter

ΔI	Peal-to-Peak input current of the six-legs DC/DC converter
ΔVo	Peal-to-Peak of the AC component of the output voltage of the six-legs DC/DC converter
E_{acc}	Energy required during acceleration phase
E_{brak}	Energy required during braking phase
fs	Switching frequency of a power switch of the six-legs DC/DC converter
$G(s)$	Closed loop transfer function of the six-legs DC/DC converter
$G_v(s)$	Transfer function in Laplace domain of the output voltage versus the duty cycle of the six-legs DC/DC converter
$G_{iL}(s)$	Transfer function in Laplace domain of the current through an inductor versus the duty cycle of the six-legs DC/DC converter
$\bar{I}$	Mean value of the current
I_D	Current flowing through a diode of the six-legs DC/DC converter
I_{DS}	Rated current of a power switch of the six-legs DC/DC converter
I_L	Current flowing through an inductor of the six-legs DC/DC converter
Irr	Reverse Recovery current of a diode of the six-legs DC/DC converter
KI	cancellation factor
L_{CCM}	Minimum value of the inductor to guarantee the CCM operation of the six-legs DC/DC converter
L	Inductor of the six-legs DC/DC converter
N	Number of legs of the six-legs DC/DC converter
P_{conv}	Rated power of the six-legs DC/DC converter
Pc	Power losses for a power switch of the six-legs DC/DC converter during conduction
Pc_c	Power losses on the output capacitor of the six-legs DC/DC converter
P_{D_cond}	Power losses for a diode of the six-legs DC/DC converter during conduction
P_{D_rr}	Power losses for a diode of the six-legs DC/DC converter due to reverse recovery
$PI_i(s)$	Proportional Integral regulator of the current of the six-legs DC/DC converter
$PI_v(s)$	Proportional Integral regulator of the voltage of the six-legs DC/DC converter
Rds(on)	Conduction resistance of a power switch of the six-legs DC/DC converter
R_D	Conduction resistance of a diode of the six-legs DC/DC converter
P_{SW}	Power losses for a power switch of the six-legs DC/DC converter during switching
Resr	Parasitic resistance of the output capacitor of the six-legs DC/DC converter
R_L	Parasitic resistance of an inductor of the six-legs DC/DC converter
ton	Turn-on time of a power switch of the six-legs DC/DC converter
toff	Turn-off time of a power switch of the six-legs DC/DC converter
trr	Reverse recovery time for a diode of the six-legs DC/DC converter
Vo	Output voltage diode of the six-legs DC/DC converter
VDSS	Maximum drain-source rated voltage of a power switch of the six-legs DC/DC converter
VSC	Voltage across the terminal of the supercapacitor
Vγ	Threshold voltage of a diode of the six-legs DC/DC converter

Author Contributions: Conceptualization, Gianpaolo Vitale and Emiliano Pipitone; Formal analysis, Gianpaolo Vitale and Emiliano Pipitone; Investigation, Gianpaolo Vitale and Emiliano Pipitone; Methodology, Gianpaolo Vitale and Emiliano Pipitone; Writing – original draft, Gianpaolo Vitale and Emiliano Pipitone.

Conflicts of Interest: The authors declare no conflict of interest.

References

1. Iodice, P.; Senatore, A. Road transport emission inventory in a regional area by using experimental two-wheelers emission factors. In: World Congress on Engineering. 2013. p. 2078-0958.

2. Iodice, P., et al. Air pollution monitoring using emission inventories combined with the moss bag approach. Science of the total environment, 2016, 541: 1410-1419.
3. Pipitone, E.; Beccari, A. A Study on the Use of Combustion Phase Indicators for MBT Spark Timing on a Bi-Fuel Engine. SAE Technical Paper, 2007.
4. Bue, F., et al. Misfire detection system based on the measure of crankshaft angular velocity. In: Advanced Microsystems for automotive applications. 2007. p. 149-161.
5. Cammalleri, M.; Sorge, F. Approximate closed-form solutions for the shift mechanics of rubber belt variators. In: ASME 2009 International Design Engineering Technical Conferences and Computers and Information in Engineering Conference. American Society of Mechanical Engineers, 2009. p. 187-196.
6. Cammalleri, M. Efficiency of split-way CVT's. A simplified model. SAE Technical Paper, 2007.
7. Lequesne, B. Automotive electrification: The nonhybrid story. IEEE Transactions on Transportation Electrification, 2015, 1.1: 40-53.
8. Szumanowsky, A.; Liu, Z.; Krawczyk, P. Analyse of clutch-brake system control based on experimental tests and applied in hybrid power train. World Electric Vehicle Journal, 2013, 6.2: 353-363.
9. Huh, J.; Oh, K.; Shin, D. Study of regenerative breaking control for HEV with multispeed transmission. World Electric Vehicle Journal, 2015, 7.2: 278-286.
10. Choi, J. et al. Analysis of regenerative braking effect to improve fuel Economy for E-REV bus based on simulation. World Electric Vehicle Journal, 2015, 7.3: 366-370.
11. Itani, K.; et al. Regenerative braking modeling, control, and simulation of a hybrid energy storage system for an electric vehicle in extreme conditions. IEEE Transactions on Transportation Electrification, 2016, 2.4: 465-479.
12. Kloetzl, J.; Gerling, D. An interleaved buck-boost-converter combined with a supercapacitor-storage for the stabilization of automotive power nets. In: 2011 IEEE Vehicle Power and Propulsion Conference. IEEE, 2011. p. 1-6.
13. N. Shah, D. Czarkowski, Supercapacitors in Tandem with Batteries to Prolong the Range of UGV Systems, Electronics 2018, 7, 6; doi:10.3390/electronics7010006.
14. Akar, Furkan, et al. A bidirectional nonisolated multi-input DC–DC converter for hybrid energy storage systems in electric vehicles. IEEE Transactions on Vehicular Technology, 2016, 65.10: 7944-7955.
15. Vitale, G. Supercapacitor modelling by Lagrange's equations. In: International conference on modern electrical power engineering, (ICMEPE-2016). 2016. p. 1-6.
16. Huang, Y. et al. An Efficient Energy Regeneration System for Diesel Engines. World Electric Vehicle Journal, 2010, 4.3: 525-531.
17. Cheali, E., et al. Electrochemical and electrostatic energy storage and management systems for electric drive vehicles: State-of-the-art review and future trends. IEEE Journal of Emerging and Selected Topics in Power Electronics, 2016, 4.3: 1117-1134.
18. Zhang, J. et al. Regenerative braking system for series hybrid electric city bus. World Electric Vehicle Journal, 2008, 2.4: 363-369.
19. Wen, M. T. X. ; Tien, D. T. K. Analysis of a Hybrid Mechanical Regenerative Braking System. In: MATEC Web of Conferences. EDP Sciences, 2018. p. 02011.
20. Barlow, T. J., et al. A reference book of driving cycles for use in the measurement of road vehicle emissions. TRL Published Project Report, 2009. online available: https://assets.publishing.service.gov.uk/government/uploads/system/uploads/attachment_data/file/4247/ppr-354.pdf.
21. Tsodoulis, S. N.; Safacas, A. N. Analysis of a drive system in a fuel cell and battery powered electric vehicle. International Journal Of Renewable Energy Research, 2011, 1.3: 140-151.
22. Addula, S. R.; Mahalingam, P. Coupled inductor based soft switched interleaved dc-dc converter for pv applications. International Journal of Renewable Energy Research (IJRER), 2016, 6.2: 361-374.
23. Kolar, J. W., et al. Extreme efficiency power electronics. In: 2012 7th International Conference on Integrated Power Electronics Systems (CIPS). IEEE, 2012. p. 1-22.
24. Roberto, S. F., et al. Equivalent Circuit Modelling of Ferrite Inductors Losses. In: 2018 IEEE 4th International Forum on Research and Technology for Society and Industry (RTSI). IEEE, 2018. p. 1-4.
25. Giglia, G. , et al. Automatic EMI filter design for power electronic converters oriented to high power density. Electronics, 2018, 7.1: 9.

384 26. Durán, E., et al. An Application of Interleaved Zeta-Buck-Boost Combination Converter in Distributed
385 Generation. In: International Congress on Engineering and Sustainability in the XXI Century. Springer,
386 Cham, 2017. p. 291-304.
387 27. Hegazy , O.; Van Mierlo, J.; Lataire, P. Analysis, control and comparison of DC/DC boost converter
388 topologies for fuel cell hybrid electric vehicle applications. In: Proceedings of the 2011 14th European
389 Conference on Power Electronics and Applications. IEEE, 2011. p. 1-10.

390